JOURNAL OF MATERIALS SCIENCE **35** (2000) 2807–2814

Alumina-mullite-zirconia composites obtained by reaction sintering

Part I *Microstructure and mechanical behaviour**

A. C. MAZZEI, J. A. RODRIGUES
Department of Materials Engineering, Universidade Federal de São Carlos, São Carlos, S.P., Brazil
E-mail: pmazzei@iris.ufscar.br

Zirconia particles can be added to the matrix to overcome the brittleness inherent in ceramic materials, thereby strengthening the material through tetragonal-monoclinic phase transformation of the zirconia. This work focuses on the effect of the percentage of zirconia and mullite in the mechanical and thermomechanical properties of alumina-mullite-zirconia composites that were obtained by reaction sintering of alumina and zircon. Different samples were processed, resulting in composites with an alumina matrix, which was always volumetrically predominant. A percentage of alumina and mullite with maximized mechanical and thermomechanical properties was observed. This maximization is discussed in terms of the microstructure obtained for the composites mentioned above. The toughening mechanisms provided by zirconia and mullite inclusions, based not only on the *R*-curve behaviour but also on the analysis of the fracture surface, are also discussed in this report. An additional paper will be forthcoming, containing detailed discussions concerning the *R*-curve behaviour of the same composites.

1. Introduction

Alumina-based ceramics show high values of refractoriness, hardness, strength and resistance to chemical attack, being these properties suitable for a broad range of industrial applications. However, owing to their brittleness, these ceramics are unsuitable for application in conditions of severe thermal shock or in structural applications requiring high toughness.

In order to overcome the inherent brittleness of alumina and of a great number of ceramic materials whose other properties may be useful in an industrial context (mullite for instance) some mechanisms can be incorporated in the matrix to make it tougher. An example of this is the addition of zirconia particles in a ceramic matrix [1, 2]. These particles toughen the material mainly as a consequence of the tetragonal-monoclinic phase transformation that can occur during the fracture process or during sintering cooling. In the former case, the stress induced phase transformation toughening mechanism is activated, while in the latter, the microcracks produced in the matrix as a result of the phase transformation that occurs during the sintering cooling are responsible for the increase of crack propagation energy [3, 4].

There are many ways of introducing zirconia into an alumina matrix to produce these composites, e.g. conventional or chemical processing of alumina and zirconia powders as well as sol-gel can be used. The same holds true in reaction sintering, in which alumina and zircon ($ZrSiO_4$) [5] are used as the initial powders. The latter process is a more attractive one because it is cheaper compared to the starting raw materials, zircon and zirconia, and because it can easily be implemented industrially (in view of conventional equipment and processing techniques).

In reaction sintering, a mullite matrix with zirconia inclusions or an alumina matrix with mullite and zirconia inclusions can be obtained as the resulting microstructure; in the latter case an additional toughening mechanism is present in the matrix (bridging) if the mullite inclusions appear in a needle shape. The disadvantage of using reaction sintering is that the dissociation reaction of zircon causes porosity that may lead to degradation of the mechanical properties. In a attempt to control this porosity, two sintering steps rather than one can be used. If two sintering steps are taken, the first step is densification of the composite and the second, reaction [6, 7]. When only one sintering step is carried out, densification and reaction occur simultaneously. However, Folgueiras [7] observed porosity in both the one and the two-step sintering processes. According to this author, the porosity produced in the reaction step reduced the densification produced in the first step. For that reason, this work uses the one-step

* Based in part on the Thesis submitted by A. C. Mazzei for the MSc. degree in Materials Engineering, Graduate Program, Universidade Federal de São Carlos, São Carlos, SP, Brazil, 1997. Supported by CAPES, CNPq and FAPESP.

TABLE I Amounts of alumina and zircon used to produce the composites and concentration of Al_2O_3, ZrO_2 and mullite calculated by Equation 1

	Raw materials (weight %)		Concentration of Al_2O_3, ZrO_2 and mullite in the composites (weight % (vol %))		
Composite designation	Al_2O_3	$ZrSiO_4$	Al_2O_3	ZrO_2	Mullite
0	100	0	100	0	0
Pure alumina			(100)	(0)	(0)
1	95	5	89.47	3.87	6.67
			(88.45)	(2.67)	(8.88)
2	90	10	79.07	7.67	13.26
			(78.17)	(5.31)	(16.52)
3	85	15	68.85	11.41	19.74
			(67.69)	(7.86)	(24.45)
4	80	20	58.79	15.09	26.12
			(57.49)	(10.34)	(32.17)
5	75	25	48.89	18.71	32.40
			(47.55)	(12.75)	(39.70)

reaction sintering process to obtain alumina-mullite-zirconia composites.

The mechanical properties such as the modulus of rupture (σ_f), Young's modulus (E), and fracture toughness (K_{IC}) can be measured to evaluate the effect of zirconia and mullite inclusions in the alumina matrix. Besides the analysis of these properties, it is also meaningful to evaluate the R-curve behaviour of the composites. The resistance to crack growth can be verified in the R-curve, which shape helps to identify the presence or absence of possible toughening mechanisms [8] provided by the mullite and zirconia inclusions. In this issue of the toughening mechanisms, it is also worthwhile including the analysis of the total work of fracture (γ_{wof}), representing the average difficulty for crack propagation to occur in the composite, as well as an analysis of the surface fracture resulting from stable crack propagation. These evaluations have a tendency to confirm as well as improve analyses of the toughening mechanisms obtained from the R-curve behaviour of the composites.

When considering the performance of the composites in thermal shock applications, not only the R-curve behaviour but also an analysis of the total work fracture are important. However, should the use of alumina-mullite-zirconia composites become feasible for the aforementioned applications, some of their thermal shock properties must be characterized. As a preliminary evaluation, the variation of critical temperature for initiation of crack propagation (ΔT_c) and thermal shock damage resistance (R'''') can be calculated from the equations that use the linear thermal expansion coefficient (α_{th}) and the mechanical properties.

It is just as important to know the variations of the properties mentioned earlier according to the amount of mullite and zirconia inclusions as it is to evaluate them, since the efficiency of the toughening mechanisms is a result of the percentage of these inclusions in the matrix. Thus, the purpose of this study is to show the mechanical and thermomechanical property variations, as well as the variation of the R-curve behaviour resulting from the amount of mullite and zirconia inclusions in the alumina matrix. A discussion of the toughening mechanisms is also presented.

2. Experimental procedure

Alumina A-16 SG[†] and zircon A-200[‡] powders were used in the preparation of the alumina-mullite-zirconia composites. These powders were mixed in a ball mill with water and DISPERSAL B-130[§] as deflocculant. The zircon powder used in the mixture was previously settled and ball milled to obtain a powder with an average particle size of 2 μm. The suspensions obtained in the mixture process were spray dried.

Six different compositions were processed with the purpose of examining the mechanical and thermomechanical property variations resulting from the percentage of the zirconia and mullite inclusions in the alumina matrix. Table I lists the alumina, zirconia and mullite contents that were calculated for each sample, according to the chemical reaction equation between alumina and zircon described by Equation 1. This table also shows the amount of zircon that was used in the reaction (Equation 1) for each sample.

$$(3+x)Al_2O_3 + 2ZrSiO_4 \rightarrow x\,Al_2O_3 + 2ZrO_2 + 3Al_2O_3 \cdot 2SiO_2 \quad (1)$$

Our work with the dried mixtures involved the use of $62.0 \times 5.0 \times 6.0$ mm^3 bars pressed under 60 MPa, while the sintering process was carried out in one 2-hour sintering step at 1650°C. The heating ramp rate used was 10°C/min. After completion of the sintering process, bulk density and porosity were measured by the water-immersion method. The polished and thermally etched samples (1550°C) were examined using a scanning electron microscope (SEM—Model 440, Leica Cambridge, England) and X-ray diffraction (Model D 5000, SIEMENS, Karls Hüre, Germany) to define the microstructural characterization.

2.1. Mechanical properties

All the mechanical tests were carried out in an MTS machine (810 series, with a 458.20 controller,

[†] ALCOA S/A, Poços de Caldas, MG, BR.

[‡] Nuclemon, Barra Funda, SP, BR.

[§] Ammonium Polyacrylate, AQUATEC, São Paulo, SP, BR.

Minneapolis, USA) using three-point bending. The four-point bending test was not considered due to the extreme difficulty in obtaining stable crack propagation in pure alumina samples even with the Chevron notch.

The modulus of rupture (σ_f) was obtained from a load-deflection curve (P vs. δ), which was reached by catastrophic propagation, using samples without notches. To calculate this property, the following Equation [9] was used:

$$\sigma_f = \frac{3}{2} \cdot \frac{P_{max} \cdot S_1}{b \cdot w^2} \quad (2)$$

where P_{max} is the peak load of the P vs. δ-curve, S_1 is the support span and b and w are the width and the height of the bar, respectively.

Samples without notches were also used to determine Young's modulus, although, in this case, a lever type extensometer was used to measure bar deflection without the influence of the machine and test devices. The value of E was calculated by the following equation:

$$E = \frac{S_1^3}{4 \cdot b \cdot w^3} \cdot m \quad (3)$$

where m is the slope of the tangent line to the initial straight portion of the load-deflection curve.

On the other hand, to determine K_{IC}, a straight-through notch with a depth of only 30% of w was produced in all the specimens in order to reach the condition of catastrophic propagation. A 150 μm thick diamond disc was used to machine this notch. The value of K_{IC} was calculated using the following Equation [9]:

$$K_{IC} = \frac{P_{max}}{bw^{1/2}} \cdot y(\alpha_0), \quad (4)$$

where α_0 is the initial relative depth of the notch given by a_0/w, considering a_0 as the original depth of the notch, and $y(\alpha)$ is a geometrical factor that is dependent on $\alpha = a/w$, where a is the instantaneous crack length. The $y(\alpha)$ function describes the influence of the notch and test geometry on the fracture toughness. Considering a straight-through notch and three-point bending test, $y(\alpha)$ is given by Equation 5 [9].

$$y(\alpha) = \frac{S_1}{w} \cdot \left[\frac{3\alpha^{1/2}}{2(1-\alpha)^{3/2}}\right] \cdot \left\{1.99 - 1.33\alpha - (3.49 - 0.68\alpha + 1.35\alpha^2) \cdot \left[\frac{\alpha(1-\alpha)}{(1+\alpha)^2}\right]\right\} \quad (5)$$

In Equation 4, the value of $y(\alpha)$ is calculated considering $\alpha = \alpha_0$ in Equation 5.

2.2. *R*-Curve behaviour and total work of fracture

The R-curve was calculated based on the equations of linear elastic fracture mechanics, while the instantaneous relative crack length ($\alpha = a/w$) was obtained by the change in compliance [10, 11]. These α values were calculated from the P vs. δ-curves, obtained under stable crack propagation and continuous loading conditions. The three-point bending test was used. In order to facilitate stable crack propagation, Chevron notched bars with the notch tip at 35% of w, and a slow rate of actuator motion (1 μm/min) were used.

For the P vs. δ-curves mentioned above, the values of α were calculated by numerical integration of Equation 6, which has already been adapted to the Chevron notch [12, 13].

$$C(\alpha) - C(\alpha_0) = \frac{2}{b \cdot E} \cdot \int_{\alpha_0}^{\alpha} y^2(\alpha) \cdot \left(\frac{\alpha_1 - \alpha_0}{\alpha - \alpha_0}\right) \cdot d\alpha \quad (6)$$

where, $C(\alpha)$ is the instantaneous compliance defined as δ/P, and α_1 is the relative depth at which the crack changes from the Chevron to the straight-through geometry. If $\alpha \geq \alpha_1$ the expression between brackets is replaced by 1.0. α is achieved iteractively from the comparison between the calculated values for $C(\alpha)$ with those obtained experimentally (from the P vs. δ-curves). Thus, it is possible to calculate the instantaneous stress intensity factor, $K_1(\alpha)$, and crack resistance, $R(\alpha)$, using Equations 7 and 8, respectively. As a result, K_1 vs. α and R vs. α curves can be defined.

$$K_I(\alpha) = \left(\frac{P}{b \cdot w^{1/2}}\right) y(\alpha) \left[\frac{\alpha_1 - \alpha_0}{\alpha - \alpha_0}\right] \quad (7)$$

$$R(\alpha) = \frac{K_I^2(\alpha)}{E} \quad (8)$$

This iterative process to calculate α and to obtain the C vs. α, K_1 vs. α and R vs. α curves was carried out using a Visual Basic program developed by Zamprogno [14].

The value of the total work of fracture, γ_{wof}, was obtained from the area under the P vs. δ-curves used to calculate the R-curves, divided by twice the corresponding projected fracture area.

Five specimens from each composition were used for all the tests in order to define possible measurement errors. The fracture surfaces obtained under stable crack propagation conditions were observed in SEM.

2.3. Thermal shock properties

The variation of critical temperature for initiation of crack propagation (ΔT_c) and thermal shock damage resistance (R'''') were evaluated based on the mechanical properties measured and on the equations below:

$$\Delta T_c = \frac{\sigma_f \cdot (1 - \upsilon)}{E \cdot \alpha_{th}} \quad (9)$$

$$R'''' = \frac{\gamma_{wof} \cdot E}{\sigma_f^2 \cdot (1 - \upsilon)} \quad (10)$$

where υ is Poisson's ratio, which has been considered in this work as equal to 2.5 for all samples; and α_{th} is the linear thermal expansion coefficient, which was obtained through dilatometric measurements (Orton Automatic Recording Dilatometer, Model 1500°C, Ohio, USA) of each sample.

3. Results and discussions

3.1. Physical and microstructural characterization

Table I shows an increase of zirconia and mullite concentrations in the allumina matrix as zircon is added to the reaction. One can also see that zirconia always constitutes the minor phase in the composite.

Fig. 1 depicts the results of the characterization of porosity and density. The same figure shows that an increase in the zircon content in the reaction (given by Equation 1) increases porosity and lowers density. The drop in bulk density can be explained by two factors: first, as a consequence of increased porosity, and second, as a result of the increased amount of mullite phase (Table I), which is less dense than alumina (see the drop of the theoretical density curve, which was calculated considering a simple rule covering the mixture of different phases in Fig. 1). Increased porosity occurs mainly as a result of the zircon's dissociation reaction. This is confirmed by Fig. 1, which shows that the bulk density curve and the theoretical density curve are not parallel, since the disparity between the curves increases as the amount of zircon in the reaction increases. There is also some porosity coming from the processing steps; however, if pure alumina is taken as reference to measure this porosity, it can be noted that this value is not above 1% (Fig. 1).

SEM observations of the composites' polished surfaces confirmed the increased porosity, measured by the water-immersion method, as shown in the sequence of micrographs in Figs 2a, b and c. An increased amount of zircon in the reaction (composites 4 and 5, Table I) showed microcracks in the alumina matrix and pore coalescence, as illustrated in Fig. 2c.

Observation of the micrographs also enables us to describe the composites' microstructure. The matrix shows a homogeneous distribution of mullite and zirconia inclusions (resulting from the good homogeneity achieved in the mixing process and from the use of zircon with a small average particle size). Moreover, the mullite inclusions are preferentially in the equiaxial morphology and are therefore indistinguishable from alumina grains. The incidence of mullite in the acicular morphology was low because no processing aid or resource was used that could aid the formation of this

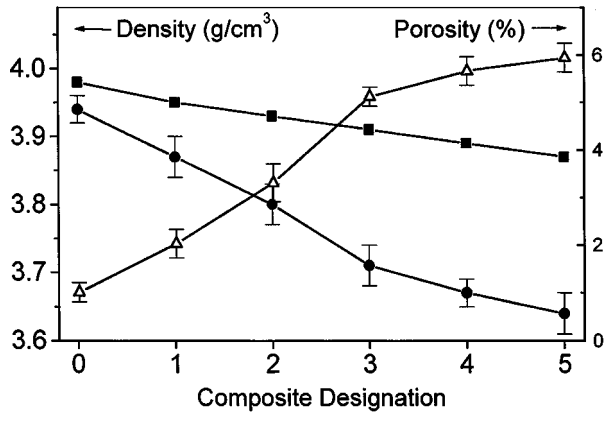

Figure 1 Variation of the theoretical density (—■—), bulk density (—●—) and porosity (—△—) based on the amount of zircon into the reaction, represented here as the composite designation (see Table I).

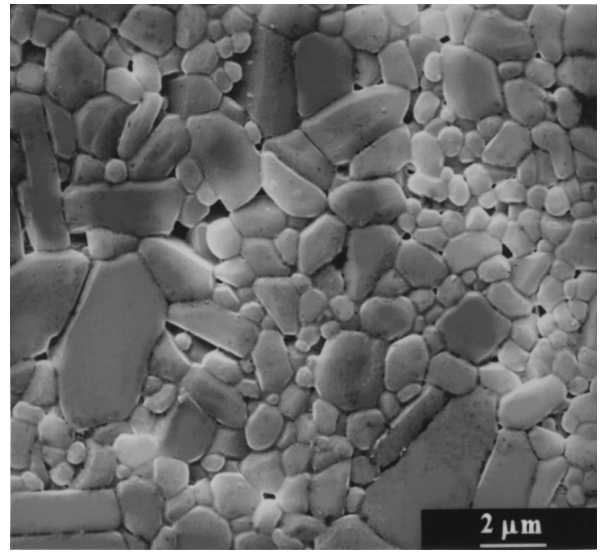

(a)

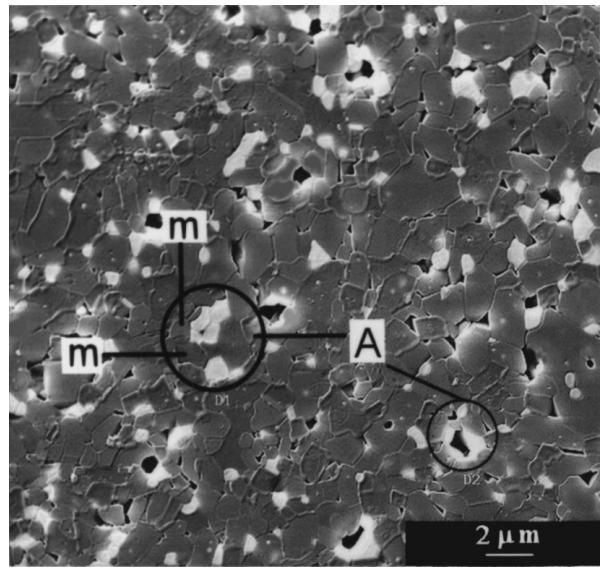

(b)

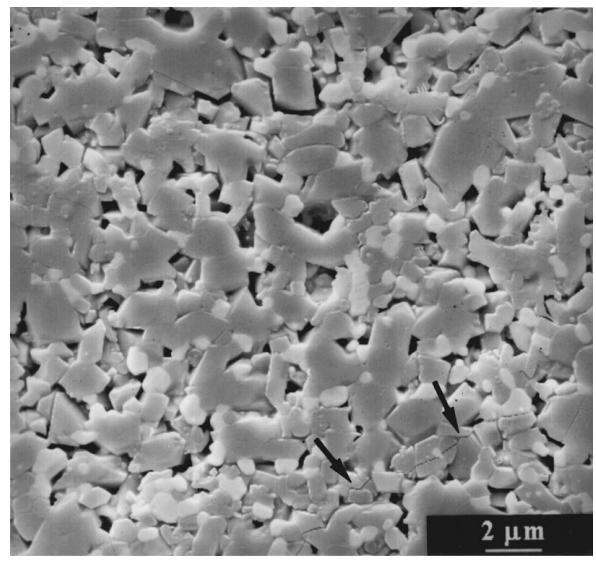

(c)

Figure 2 Micrographs of polished surfaces. (a) Pure alumina; (b) Composite 3; and (c) Composite 5. Note, in (b), the structure formed by the dissociation reaction (label A and mullite grains, label m), and in (c), the microcracks in the matrix indicated by arrows.

morphology. An EDS analysis (Energy Dispersive Spectroscopy—Link, Model eXLII, Oxford, England) was used to distinguish the alumina and mullite phases, and image analysis used to quantify them. The results obtained from the image analysis (Leica, Model Q-600, Cambridge, England) follow the prediction of Equation 1, shown in Table I (error less than 5%). As regards the average grain size, values of 4.0 μm, 3.0 μm and 1.0 μm were obtained for the zirconia, mullite and alumina respectively. Lastly, it is worthwhile to note the typical structure, which is formed by the alumina and zircon sintering reaction (labeled "A" in Fig. 2b): an alumina matrix with zirconia inclusions surrounded by mullite grains (labeled "m" in Fig. 2b), and the presence of pores.

X-ray diffraction characterisation of the composites confirmed an increase in the quantity of zirconia and mullite phases with increasing amounts of zircon in the reaction. No other phase was found, such as impurities or zircon; only the alumina, mullite and zirconia (tetragonal and monoclinic phases) were identified.

3.2. Mechanical properties and *R*-curve characterisation

The variation of mechanical properties with sample composition is given in Table II, while Fig. 3 shows the *R*-curves for all of the composites. Each *R*-curve shown represents the average of the data from 5 different specimens of the same composition.

The maximum values of K_{IC}, σ_f and γ_{wof} (Table II) are obtained with composite 3, followed by a strong drop in these values for composites 4 and 5. The same behaviour is present in the *R*-curves (Fig. 3), which means that composite 3 has better *R*-curve behaviour than the other composites.

TABLE II Mechanical properties obtained for the composites

Composite designation	σ_f (MPa)	K_{IC} (MPa·m$^{1/2}$)	E (GPa)	γ_{wof} (J/m^2)
0	332 ± 25	5.34 ± 0.28	378 ± 42	34 ± 4
1	295 ± 20	5.25 ± 0.14	296 ± 10	50 ± 3
2	295 ± 37	5.41 ± 0.31	295 ± 12	52 ± 3
3	317 ± 35	5.57 ± 0.03	255 ± 44	67 ± 3
4	204 ± 65	3.54 ± 0.22	173 ± 6	55 ± 3
5	118 ± 20	3.36 ± 0.14	178 ± 30	36 ± 2

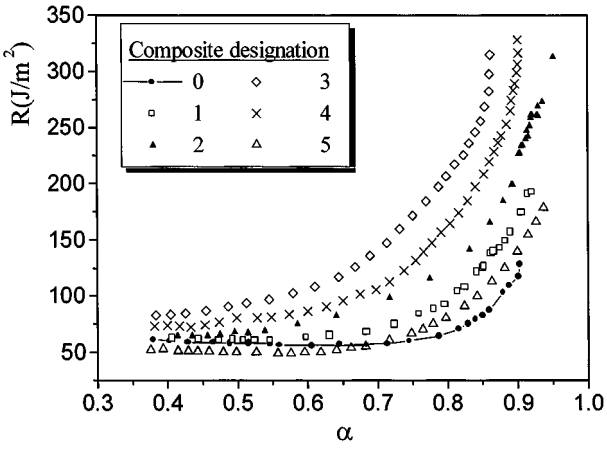

Figure 3 *R*-curves obtained for the composites. Each *R*-curve represents the average data of 5 different specimens of the same composite. Three-point bending and Chevron notch were used.

As regards σ_f, two parameters can be cited that influence this property that are also present in the composites: the porosity and the toughening mechanisms obtained from the zirconia and mullite inclusions. In composites 1 and 2, there was a light fall in σ_f (in relation to the pure alumina), which reflects the increase of porosity caused by the sintering reaction (as discussed in the previous item). In composite 3, σ_f increases even with the increase in porosity (Fig. 1), as a result of the strengthening caused by zirconia inclusions in the alumina matrix. On the other hand, in composites 4 and 5, a strong degradation of σ_f was observed. This occurred as a consequence of the high pore concentration, pore coalescence and due to the presence of microcracks in the matrices of these composites (see Fig. 2c). Nonetheless, it is worth mentioning that the σ_f of sample 3 is higher than that of the pure alumina, despite the fact that there is increased porosity.

Similarly, as a result of the porosity and zirconia inclusions, K_{IC} showed the same trend as σ_f, reaching a maximum in composite 3, which also was higher than the value for pure alumina. The values of K_{IC} are generally, however, overestimated due to the thick notch used. Machining with a diamond disc 150 μm thick produces a notch of width approximately 170 μm.

As for Young's modulus, it is known that it can generally be considered as the sum of Young's modulus of each phase present in the composite, according to its volumetric fraction. This may explain the continuous fall in E (Table II), since zirconia and mullite phases have lower E-values than alumina. Moreover, as discussed earlier, porosity increases in proportion to the increased amount of zircon in the reaction, and this causes a further decrease of the E values. A significant drop in the values of this property for composites 4 and 5 was also observed, as a result of pore coalescence and microcracking in the matrix.

With regard to the *R*-curve behaviour, it can be stated that the presence of zirconia and mullite inclusions strengthened the material, and that the best results were also obtained in composite 3. In pure alumina, the *R*-curve is flat until the value of α becomes equal to 0.8. Composites 1 and 2 showed a slight improvement not only in the initial level of the *R*-curve but also in the increasing behaviour of the *R*-curve. The highest increase of *R* occurred in composite 3, followed by a drop of the *R*-curve level in composites 4 and 5. It can also be noted, in Fig. 3, that the initial level of the *R*-curve in composite 5 was below the level of the *R*-curve of pure alumina, evidencing the microstructure's degradation in terms of strength, caused by increased porosity. The strong increase of *R* to α higher than 0.8, as observed in the curves of Fig. 3, is attributed to the influence of the $y(\alpha)$ function (Equation 5) used in the calculations. This region of α cannot be used to discuss the *R*-curve behaviour, however, but will be discussed in detail in a forthcoming article [15].

The composites' improved *R*-curve behaviour can be observed in to two factors: a) the significant increase in crack propagation initiation energy, which was also

observed in the K_{IC} values (which caused the initial level of the *R*-curve to rise); and b) the considerably increased *R*-curve inclinations in the region in which the pure alumina has a flat *R*-curve. This indicates that there are toughening mechanisms in the composites, where the process zone (wake zone) grows continuously with crack propagation as, for instance, in crack branching. The above example is in complete harmony with the significant increase of γ_{wof} values up to composite 3 (see Table II).

The fracture surfaces were analyzed to investigate the presence of these composite toughening mechanisms. Fig. 4 illustrates our findings for composite 3. As seen in Fig. 4a, the zirconia tetragonal-monoclinic phase transformation occurred during the sintering cooling, producing microcracks in the matrix that may be responsible for the crack branching. An evaluation of pure alumina samples revealed that this type of microcrack is not present in the fracture surface grains. That is why we believe that the microcracks shown in Fig. 4a, although modified by the fracture process, were produced by the zirconia inclusions. In Fig. 4b, the microcracks that surround the grains indicate that the branching of the crack actually occurred. It is also clear that intergranular fracture occurred, which, owing to the grain-bridging interaction, also enhances the work of fracture. Thus, our evaluations of the micrographs and analysis of the *R*-curve shape led us to conclude that the main toughening mechanism acting in the composites appears to be crack branching caused by the microcracking of the matrix by the tetragonal-monoclinic phase transformation of zirconia. Other toughening mechanisms may occur, albeit to a lesser extent, such as stress-induced phase transformation (to a lesser extent, because zircon powder instead of PSZ was used as raw material, and also since the X-ray diffraction analysis revealed

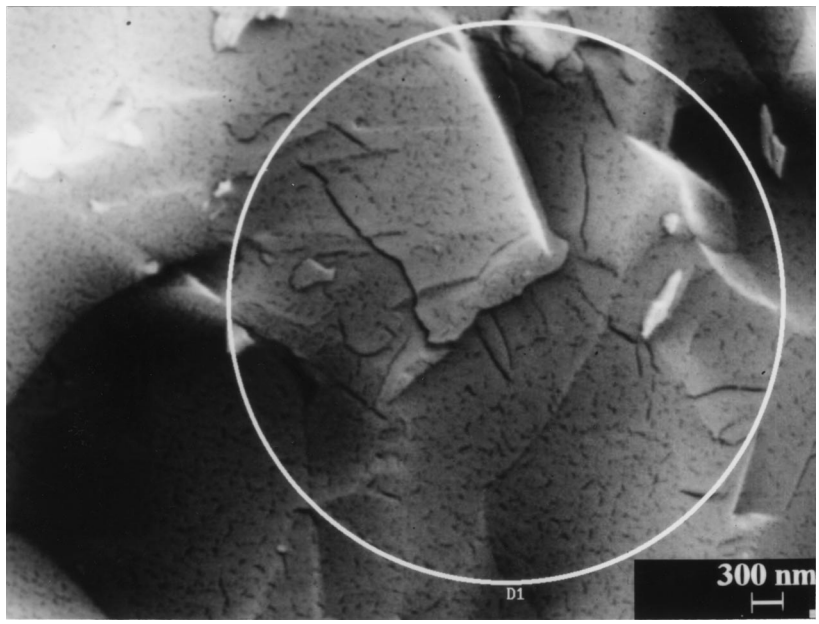

(a)

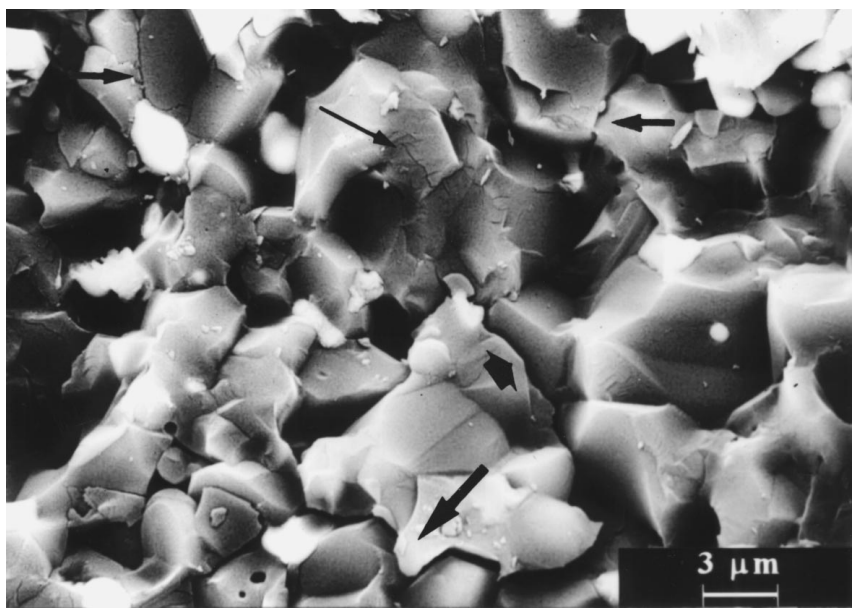

(b)

Figure 4 Micrographs of the fractured surfaces from composite 3 observed in the MEV. (a) Note the microcracks (inside the circle) produced by the tetragonal → monoclinic phase transformation during sintering cooling. (b) Note the arrows pointing to the microcracks and crack branching.

mostly the presence of the monoclinic zirconia phase); crack deflection, resulting from the presence of zirconia and mullite grains; and bridging, due to the presence of the mullite's acicular morphology (keeping in mind that there was a low incidence of this morphology in the composites).

The R-curve behaviour is in agreement with the values of γ_{wof} given in Table II. This property provides the average energy to produce a unit of fractured surface. It can be noted that, in both the R-curve and the γ_{wof}, the efficiency of the toughening mechanisms are based on the concentrations of zirconia and mullite inclusions in the alumina matrix. This efficiency is higher to composite 3 and drops down to far lower levels in composites 4 and 5, as a result of the weakening of the matrix caused by increased porosity and microcracking.

3.3. Evaluation of the thermomechanical properties

Table III shows the measured α_{th} and the evaluated R'''' and ΔT_c.

A monotonic decrease for α_{th} was obtained by increasing the amount of zircon in the reaction. This variation can be attributed to the increase of phases with lower linear thermal expansion coefficients in the alumina matrix, and as a consequence of the increased porosity, which, in turn, resulted from the alumina-zircon reaction sintering process. The value of α_{th} drops by almost 16% in relation to the pure alumina, in composite 5.

Regarding the thermomechanical properties, a higher ΔT_c was observed in composite 3, while an improved R'''' was observed in composite 5. The maximization of ΔT_c occurred in composite 3 because, as discussed before, it was in this composite that the greatest efficiency of the toughening mechanisms was achieved, as well as the best values of K_{IC} and σ_f. Table III also shows that it is in this composite that the σ_f/E ratio was maximized. As for composite 5, the low value obtained for σ_f, attributed to its high porosity, maximized the $E/(\sigma_f)^2$ ratio, resulting in the maximization of R''''. Thus, it can be observed that there are two composites for thermal shock applications: the first is composite 3, suitable when a high ΔT_c is required, and the second is composite 5, which is suitable when R'''' must be high. Hence, although R'''' has not been maximized, in dealing with composite 3 it is very important to verify that this property is 1.6 times higher than the value obtained for pure alumina, which occurs as a result of the maximization of γ_{wof}.

Working with similar composites, Folgueiras [7] measured the changes in the mechanical properties based on the intensity of thermal shock, obtaining the maximum ΔT_c of 120°C for the composite with 15% of zircon in the reaction. In the same study, she also measured the relative mechanical strength, after a one-cycle thermal shock, from which the best values obtained were for composites containing 20 and 25% of zircon in the reaction. Thus, the relative thermomechanical properties evaluated and discussed here are in agreement with those measured in her work.

4. Conclusions

It is possible to improve the mechanical behaviour of alumina through the production of alumina-mullite-zirconia composites by alumina and zircon reaction sintering.

Of all the composites produced, the most effective one appeared to be the one with 15% of zircon. This sample showed the best mechanical properties and R-curve behaviour. The improvement in these properties was attributed to the strengthening caused by the zirconia inclusions in the alumina matrix. A strong degradation of the mechanical properties and R-curve behaviour was observed in the composites with 20 and 25% of zircon, resulting from the high porosity, pore coalescence and microcracks observed in the matrix of these composites. The porosity was ascribed to the dissociation reaction of the zircon and, although it was also observed in composite 3, its extent was sufficiently low in that composite to preserve its mechanical properties and R-curve behaviour.

An analysis of the fracture surfaces indicates that the rising R-curve could be attributed to the crack branching that, in its turn, occurred due the microcracks produced in the matrix by the zirconia tetragonal-monoclinic phase transformation.

With regard to the thermomechanical properties evaluated, composite 3 also showed the best ΔT_c and a value of R'''' 1.6 times higher than the value obtained for pure alumina. The best R'''' was verified in composite 5, although this sample's mechanical properties were poor as a consequence of porosity coalescence and the presence of microcracks in the matrix.

To summarize, the characterization of the physical, microstructural, mechanical and thermomechanical properties of alumina-mullite-zirconia composites with different amounts of mullite and zirconia inclusions was carried out. Based on this set of properties, a detailed review of the composites' toughening

TABLE III Thermomechanical properties and the α_{th} evaluated for the composites

Thermomechanical properties		Composite designation					
		0	1	2	3	4	5
α_{th}	($\times 10^{-6}$°C^{-1})	8.77	8.39	8.33	7.44	7.44	7.39
σ_f/E	($\times 10^{-4}$)	8.97	9.89	10.02	12.43	11.73	6.53
ΔT_c	(° C)	78	89	90	125	118	66
$E/(\sigma_f)^2$	($\times 10^{-6}$ Pa^{-1})	3.43	3.4	3.39	2.54	4.15	12.7
R''''	($\times 10^{-4}$ m)	1.5	2.2	2.3	2.5	3.1	6.2

mechanisms was also discussed. The *R*-curves were obtained and it was observed that the shape of these curves is influenced by the $y(\alpha)$ function. These issues will be discussed in further detail in a forthcoming paper [15].

Acknowledgements

The authors would like to express their gratitude to ALCOA ALUMINIO S/A for supplying the raw material used in this study, to FAPESP, CAPES and CNPq for their financial support, and to Dr. Victor Carlos Pandolfelli for his invaluable discussions.

References

1. R. W. STEINBRECH, *J. Eur. Ceram. Soc.* **10** (1992) 131.
2. E. C. SUBARAO, in "Science and Technology of Zirconia—Advances in Ceramics, Vol. 3, edited by A. H. Heuer and L. W. Hobbs (Cleveland, Ohio, 1981) p. 1.
3. E. D. ZANOTTO and A. R. MIGLIORE, *Cerâmica* **37** (1991) 247.
4. A. G. EVANS and R. M. CANNON, *Acta Metal.* **34**(5) (1986) 761.
5. F. CAMBIER, C. BAUDIN, P. PILATI and A. LERICH, *Brit. Ceram. Trans. J.* **83** (1984) 196.
6. N. CLAUSSEN and J. JAHN, *J. Amer. Ceram. Soc.* Discussion and Notes. **63** (1980) 228.
7. M. V. FOLGUEIRAS, MSc. Dissertation, UFSCar-DEMa, São Carlos, SP, BR, 58–95, 1994.
8. M. V. SWAIN, *Materials Forum* **13**(4) (1989) 237.
9. M. SAKAI and R. C. BRADT, *Intern. Mater. Reviews* **38**(2) (1993) 53.
10. M. V. SWAIN, in "Advanced Ceramics II," Vol. 4, edited by Shigeyuki Sômia (1988), p. 45.
11. H. HÜBNER and W. JILLEK, *J. Mater. Sci.* **12** (1977) 117.
12. M. F. A. MAGON, J. A RODRIGUES and V. C. PANDOLFELLI, Proceedings of the 39th Congresso Brasileiro de Cerâmica, Águas de Lindóia-SP-BR, 1995. (Associação Brasileira de Cerâmicas, 1995) Vol. I, p. 478.
13. A. C. MAZZEI, M.Sc. Dissertation, UFSCar—DEMa, São Carlos, S.P., BR., 78–184, 1997.
14. J. A. RODRIGUES, E. R. ZAMPROGNO and V. C. PANDOLFELLI, Proceedings of the 41st Congresso Brasileiro de Cerâmicas, São Paulo, S.P., BR, 1997. (Associação Brasileira de Cerâmicas, 1998) Vol. II, p. 510.
15. A. C. MAZZEI, J. A. RODRIGUES and V. C. PANDOLFELLI, *J. Mater. Sci.* **35** (2000) 2815.

Received 3 February
and accepted 28 September 1999